Low-Voltage, Large-Scan Angle MEMS Analog Micromirror Arrays With Hidden Vertical Comb-Drive Actuators

Dooyoung Hah, Sophia Ting-Yu Huang, Jui-Che Tsai, Hiroshi Toshiyoshi, *Member, IEEE*, and Ming C. Wu, *Fellow, IEEE*

***Abstract*—This paper reports on novel polysilicon surface-micromachined one-dimensional (1-D) analog micromirror arrays fabricated using Sandia's ultraplanar multilevel MEMS technology-V (SUMMiT-V) process. Large continuous DC scan angle (23.6° optical) and low-operating voltage (6 V) have been achieved using vertical comb-drive actuators. The actuators and torsion springs are placed underneath the mirror ($137 \times 120\ \mu m^2$) to achieve high fill-factor (91%). The measured resonant frequency of the mirror ranges from 3.4 to 8.1 kHz. The measured DC scanning characteristics and resonant frequencies agree well with theoretical values. The rise time is 120 μs and the fall time is 380 μs. The static scanning characteristics show good uniformity ($< \pm 3.2\%$) for a 1 × 10 array with a mirror pitch of 150 μm. The mechanical crosstalk between adjacent mirrors is less than 37 dB. These micromirror arrays have applications in $1 \times N$ wavelength-selective switches and $N \times N$ wavelength-selective crossconnects in wavelength-division multiplexing (WDM) networks. [1048]**

***Index Terms*—Micromirror array, surface micromachining, vertical comb-drive actuator, wavelength-division-multiplexing (WDM) router, wavelength-selective switches.**

I. Introduction

ADVANCES in photonic communication networks toward optical layer networking have created a great demand for many new functional optical network elements. Microelectromechanical systems (MEMS) is a key enabling technology for many of these new photonic devices. Optical MEMS devices for dynamic optical add–drop multiplexers (OADM) [1], two-dimensional (2-D) optical crossconnects (OXC) [2]–[4], three-dimensional (3-D) OXC [5], [6], wavelength-selective switches [7]–[10], variable optical attenuators (VOA) [11], tunable wavelength filters [12], and wavelength tunable vertical-cavity surface-emitting lasers (VCSEL) [13], [14] have been reported. In this paper, we will focus on continuously scanning micromirror arrays for wavelength selective switches.

In most applications, electrostatic actuation is preferred because of its low power consumption [1]–[9], [11]–[19]. The power consideration is particularly important for systems with large arrays. Most of the micromirrors reported to date employ the parallel-plate electrostatic actuator. It is relatively simple in terms of design and fabrication; however, it suffers from the pull-in phenomenon, which limits its useful scan range. Large continuous scan angle is needed for switches with a large number of input/output (I/O) ports. Vertical comb-drive actuators reported recently [6], [8], [9], [15]–[19] offer several fundamental advantages for micromirrors. They have larger force density, which can be utilized to reduce actuation voltages. They also allow the use of stiffer springs for higher resonant frequencies without excessively high operating voltages. The pull-in instability can also be eliminated if comb geometries are chosen adequately. Bulk-micromachined structures are not suitable for micromirror arrays with high fill-factors, which often require actuators and mechanical springs to be hidden underneath mirrors. Surface-micromachining technique offers more flexibility for designing such multilayer structures.

In this paper, we report on novel surface-micromachined analog micromirror arrays with hidden vertical comb-drives for WDM applications. Large continuous scan angle (23.6° optical), low operating voltage (6 V), and high resonant frequency (3.4 kHz) have been achieved simultaneously. This paper is organized as follows: first, we describe the design and analysis of the micromirrors. We have developed a hybrid simulation technique combining a two-dimensional finite-element method (FEM) with analytic formulations, which greatly reduced the simulation time. Next, we present the fabrication of the micromirrors using Sandia's ultra-planar multilevel MEMS technology-V (SUMMiT-V) offered by Sandia National Laboratory [20]. The measurement results including DC scanning characteristics, mechanical frequency response, and transient response are described in detail. Finally, we discuss the performance of 1 × 10 micromirror arrays with high fill-factors and their applications in WDM systems.

II. Micromirror Design

The schematics of the analog micromirrors are shown in Fig. 1. The vertical comb-drives and the torsion springs are placed underneath the mirror to achieve high fill-factor, which is required to minimize the dead band in the spectral response. Two types of micromirrors were designed. Type I has one set of vertical combs underneath the mirror. Type II has two sets of vertical comb-drives at two different levels; one underneath the mirror, similar to that of Type I, and the other attached to

Manuscript received April 28, 2003; revised November 13, 2003. This work was supported by DARPA/SPAWAR under Contract N66001-00-C-8088. Subject Editor G. Stemme.

D. Hah, S. T.-Y. Huang, J.-C. Tsai, and M. C. Wu are with the Department of Electrical Engineering, University of California, Los Angeles, CA 90095 USA (e-mail: wu@icsl.ucla.edu).

H. Toshiyoshi is with the Institute of Industrial Science, University of Tokyo, Tokyo 153-8505, Japan.

Digital Object Identifier 10.1109/JMEMS.2004.825314

1057-7157/04$20.00 © 2004 IEEE

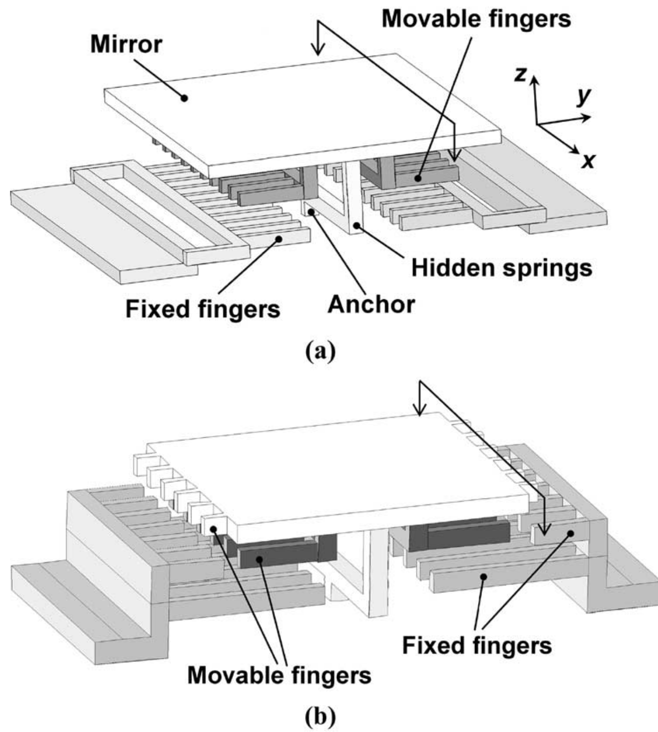

Fig. 1. The schematic views of the proposed micromirrors with hidden vertical comb-drives and springs. (a) The Type I device has one level of comb-drives and (b) the Type II device has two levels.

edges of the mirror. Fig. 2(a) and (b) show the cross-sections of both types of devices. The mirror, moving fingers, and torsion springs are connected to a ground plane. The ground plane is extended over the edges of the mirror to minimize dielectric charging effect. The actuation voltage is applied to the fixed fingers.

In contrast to the parallel-plate actuators, the analysis of the vertical comb-drive actuators is more complicated due to the presence of strong fringe fields, especially when there is no overlap between the comb fingers. We have developed a hybrid model that combines analytical formulation with 2-D finite element method (FEM). This model is much faster than full 3-D FEM, and can be used as a design tool. The total capacitance (C_t) as a function of the mirror rotation angle (θ) can be calculated by integrating the sheet capacitance (C_{unit}) of a unit cell (indicated by the dotted boxes in Fig. 2):

$$\begin{aligned} C_t(\theta) &= 2N_f \cdot \int\limits_{L_{over}} C_{\text{unit}}\left(h(y,\theta)\right) dy, \\ h(y,\theta) &= H_0 - y \cdot \theta \end{aligned} \tag{1}$$

where, N_f, $h(y,\theta)$, H_0, y, and L_{over} are the number of fingers per comb, mirror height as a function of y and θ, initial mirror height, distance from rotation axis along finger length, and overlap finger length, respectively. The factor 2 accounts for the two symmetric capacitors on both sides of a finger. $C_{\text{unit}}(h)$ is computed by 2-D FEM to include the effect of the fringe field. The electric potential distributions in the unit cell are first calculated by 2-D FEM, as shown in Fig. 2. $C_{\text{unit}}(h)$ is calculated by integrating the surface charges of the electrodes which are calculated from the potential distributions using Poisson's equation. The details will be published in [21]. The total capacitances as a function of mirror rotation angle for the Type I (finger spacing: 1 μm, finger length: 30 μm) and the Type II (finger spacing: 1 μm) devices are depicted in Fig. 3. The total capacitance of the Type I device increases rapidly at large tilt angle because of the additional parallel-plate capacitance between the mirror and the anchor pad of the fixed comb. In the Type II device, the capacitance of the upper comb increases faster at small angle than that of the lower comb because the upper comb is farther from the rotation axis, and hence it reaches its maximum value earlier [see Fig. 3(b)]. The total capacitance of the Type II device increases slowly at large angle because the anchor pads of the fixed combs are outside of the mirror area. The qualitative difference in capacitance-versus-angle $(C-\theta)$ curves also results in distinctive angle-voltage $(\theta - V)$ characteristics, as will be shown in Fig. 7. The mirror and the movable fingers are attracted toward the fixed fingers by electrostatic torque (T_e) until they are balanced by the mechanical restoring torque (T_m):

$$T_e = \frac{1}{2}V^2 \frac{\partial C_t}{\partial \theta} \tag{2}$$

$$\begin{aligned} T_m &= k_s \cdot \theta \\ &= \frac{2G_{\text{poly}} W_s^3 T_s}{3L_s}\left(1 - \frac{192}{\pi^5}\frac{W_s}{T_s}\tanh\left(\frac{\pi}{2}\frac{T_s}{W_s}\right)\right) \cdot \theta \end{aligned} \tag{3}$$

where G_{poly} is the shear modulus of polysilicon and k_s is the torsional spring constant when there are two springs, one on each side of the mirror. The dimension of the spring is $W_s(\text{width}) \times T_s(\text{thickness}) \times L_s(\text{length})$, assuming $W_s < T_s$. At sufficiently large angle, pull-in could occur due to the parallel plate capacitances between the mirror and the top surfaces of the fixed electrodes. Previously, we have proved that the pull-in angle (θ_{PI}) for any electrostatic actuator is only a function of the capacitance [22], and can be found by solving the following equation:

$$\frac{\partial C_t}{\partial \theta} - \theta \cdot \frac{\partial^2 C_t}{\partial \theta^2} = 0. \tag{4}$$

We have investigated various geometric parameters for maximizing the analog scan angles. Fig. 4(a) and (b) shows the calculated pull-in angles versus the finger spacing and length, respectively. The pull-in angle increases as the finger spacing decreases because the comb-capacitance becomes more dominant. For Type I devices, as the finger length increases, the torque due to the parasitic parallel-plate capacitance between the mirror and the anchor pads of the fixed fingers becomes larger because the pads are closer to the mirror edge. As a result, the pull-in angle decreases. On the other hand, for Type II devices, as the length of the lower finger increases, the pull-in angle increases because of the absence of the mirror-to-anchor capacitance.

Our design is based on the SUMMiT-V process. It consists of five polysilicon layers (one fixed and four movable), which is ideal for implementing our devices. There are two chemical-mechanical planarization (CMP) processes in SUMMiT-V: one before deposition of the fourth polysilicon layer (poly3) and the other before deposition of the final polysilicon layer (poly4). Table I shows the usage of the SUMMiT-V structural layers. For Type I devices, the fixed fingers consist of laminated poly 1

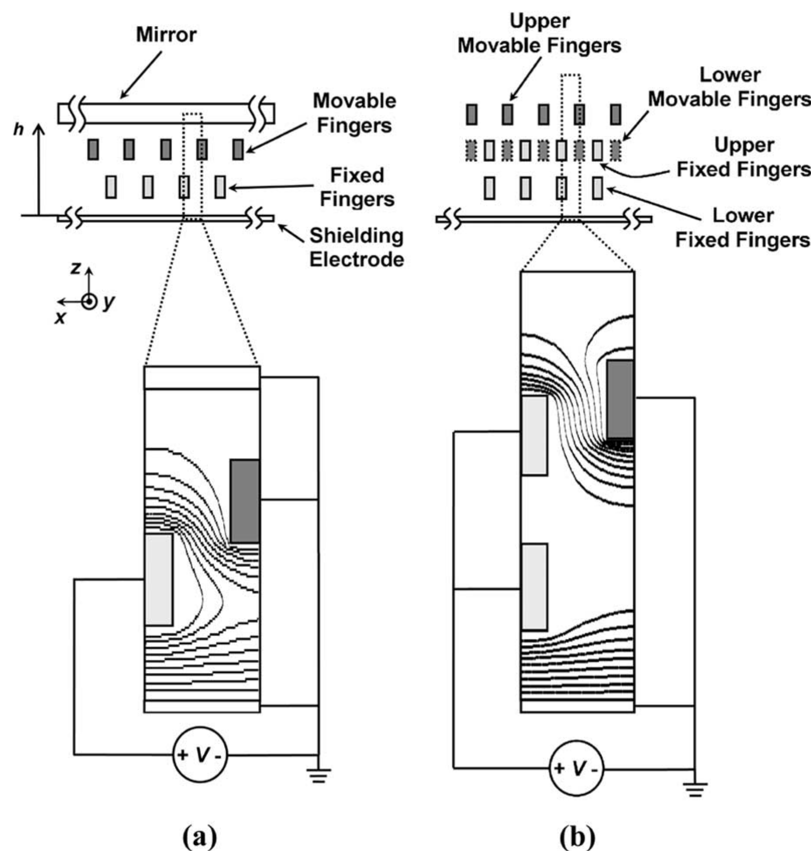

Fig. 2. The cross-section views of the (a) Type I and (b) Type II devices corresponding with the planes indicated by arrows in Fig. 1. Examples of the electric potential distributions of unit-cells (dotted box) calculated using finite element method (FEM) are depicted as well. The mirror, movable fingers, and the shielding electrode are grounded while voltages are applied to the fixed fingers.

(1 $\mu\mathrm{m}$ thick) and poly2 (1.5 $\mu\mathrm{m}$ thick) layers, and the movable fingers are made of the poly3 (2.25 $\mu\mathrm{m}$ thick) layer. The first CMP process provides a vertical offset between the fixed and the movable combs and keeps the movable fingers flat and straight. The mirror is fabricated on the top polysilicon layer, poly4 (2.25 $\mu\mathrm{m}$ thick). Thanks to the second CMP process, the underlying structures are not replicated on the mirror surface. A shielding electrode (poly0) is added below the fixed comb to prevent any unexpected interaction between the mirror and substrate. It also minimizes exposed dielectric area. Dielectric charge-up is known to cause mirror angle drift at constant voltage bias. Torsion springs are made of poly1, the thinnest structural polysilicon layer. It is anchored to the poly0 ground plane, and connected to the mirror through poly2-poly3 via and poly3-poly4 via. The cross section of the device is shown in Fig. 2(a). The assignment of the layers for Type II devices is almost the same as that of Type I devices except for the addition of the upper comb-drive. Poly4 is used for mirror and upper movable fingers. Poly3 is used for upper fixed fingers and lower movable fingers.

The minimum lateral spacing between the fixed and the movable fingers in SUMMiT-V is 0.5 $\mu\mathrm{m}$. The narrow gap spacing greatly increases the capacitance and therefore the force density, which can be utilized to reduce the operating voltage. The minimum finger width is 1 $\mu\mathrm{m}$. The narrow finger and spacing also allow us to increase the number of fingers underneath the mirror, whose width is fixed by the system requirement. Our main design tradeoff is between the operating voltage and the threshold for lateral instability. It is known that narrow gap spacing in comb drive actuators can lead to lateral instability at high voltages [23]. The narrow torsion beam permits lower operating voltage, but it also has a lower threshold for in-plane rotary pull-in. We need to have a sufficiently large safety margin to prevent lateral instability even in the presence of imperfect fabrication (e.g., misalignment between fixed and movable comb fingers). To investigate this trade-off, finger spacing ranges from 0.5 to 3 $\mu\mathrm{m}$ were included in the design. The finger length was varied from 15 to 30 $\mu\mathrm{m}$ (Type I). Three types of springs as shown in Fig. 5 are employed in our layout. An important criterion for the spring design is that the ratio of the spring constants for in-plane rotation (about z-axis), k_z, to out-of-plane rotation (about x-axis), k_x, should be as large as possible. From this point of view, a double-beam spring is better than a double-width spring because the former has smaller k_x and larger k_z. The length of the spring on each side was designed to be 55 $\mu\mathrm{m}$. The initial mirror height (H_0) is 10.75 $\mu\mathrm{m}$, which is the maximum height determined by the layer thickness of SUMMiT-V process. The mirror pitch of 150 $\mu\mathrm{m}$ is determined by the system requirement. We have incorporated lateral mechanical stoppers to prevent electric shorting in case lateral instability happens. The maximum mirror width (W_m) allowed by SUMMiT-V design rules is 137 $\mu\mathrm{m}$ for Type I and 144 $\mu\mathrm{m}$ for Type II devices. Therefore the linear fill-factor along the array direction (x) is 91% (Type I) and 96% (Type II). If we eliminate the mechanical stoppers, the maximum fill-factor would be $(149\ \mu\mathrm{m})/(150\ \mu\mathrm{m}) = 99.3\%$

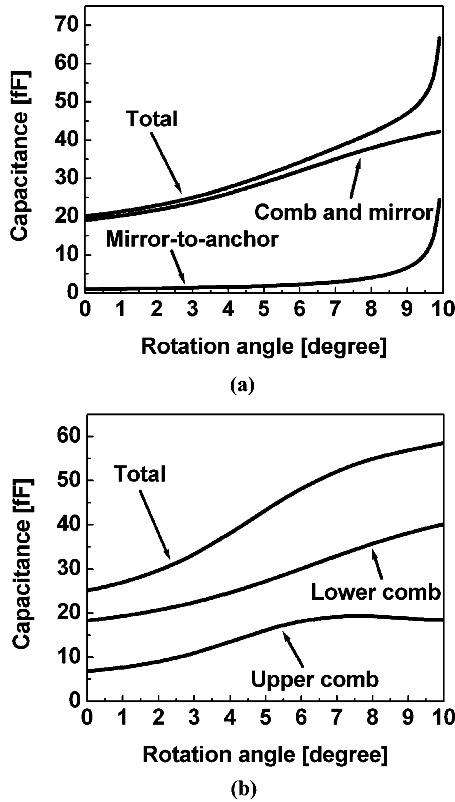

Fig. 3. The calculated capacitances as a function of rotation angle according to (1). (a) For the Type I device (finger spacing: 1 μm, finger length: 30 μm), total capacitance increases rapidly at large angle due to mirror-to-anchor capacitance. (b) The Type II device (finger spacing: 1 μm) shows S-shape transfer curve.

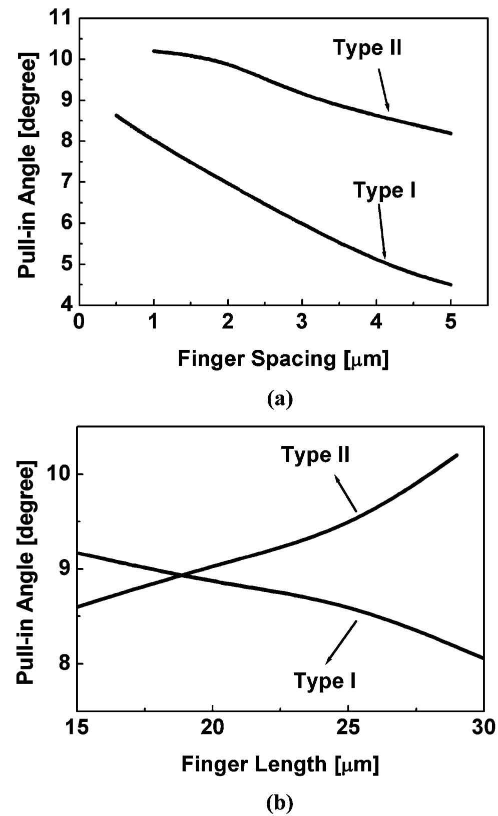

Fig. 4. The calculated pull-in angles achieved as solutions of (4) for various (a) finger spacing and (b) finger lengths (lower fingers for Type II devices).

TABLE I
USAGE OF THE SUMMiT-V POLYSILICON LAYERS IN ANALOG MICROMIRRORS

Layer	Thickness [μm]	Type I	Type II
Poly4	2.25	Mirror	Mirror
			Upper movable fingers
Poly3	2.25	Movable fingers	Upper fixed fingers
			Lower movable fingers
Poly2	1.5	Fixed fingers	Lower fixed fingers
Poly1	1.0	Fixed fingers	Lower fixed fingers
		Spring	Spring
Poly0	0.3	Shielding electrode	

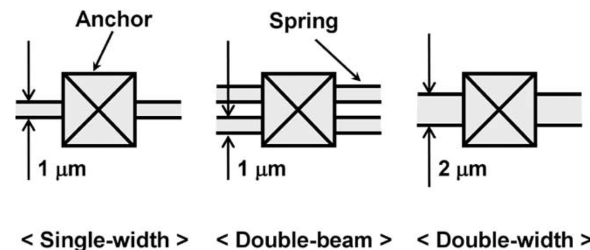

Fig. 5. Top-view schematics of the three types of torsion springs used in design.

for both types of devices. Lateral instability could be prevented by alternative spring designs as discussed above. The mirror length ($L_m = 60\ \mu\mathrm{m}$) of Type I devices was chosen to achieve a maximum mechanical rotation angle of 10° ($\approx \sin^{-1}(H_0/L_m)$). For Type II devices, the lengths of the mirror ($L_m = 30\ \mu\mathrm{m}$) and fingers (upper fingers $= 40\ \mu$m, and lower fingers $= 29\ \mu$m) were chosen to maximize the analog scan angle, at the expense of smaller mirror area. The dimensions and scan ranges of these mirrors are chosen for the optical setup of our wavelength-selective switches [24].

III. EXPERIMENTS

The fabrication of the analog micromirror arrays was performed at Sandia National Lab. After the SUMMiT-V process was completed, the chip was released in hydrofloric (HF) acid. To minimize the reflection loss from mirror surface, a metal coating is required. Aluminum and gold are two commonly used metals for this application. The presence of metal could induce electrochemical etching of polysilicon structures during the long release etch (45 min) in HF [25]. The release time is long because SUMMiT-V uses tetraethoxysilane (TEOS) oxide as sacrificial layers, which has much lower etch rate in HF compared to phosphorus-doped silicon dioxide. To prevent electrochemical etching of polysilicon, metal (Cr–Au) was deposited on the whole wafer by maskless e-beam evaporation after release. Electrical isolation between electrodes or interconnection lines was achieved by employing overhang structures which shielded the underlying structures from metal coating (see Fig. 12). The radius of curvature (R_c) before metallization was measured to be 320 ± 160 mm. The stress in metal reduces R_c to 32 ± 9 mm after metallization. Large

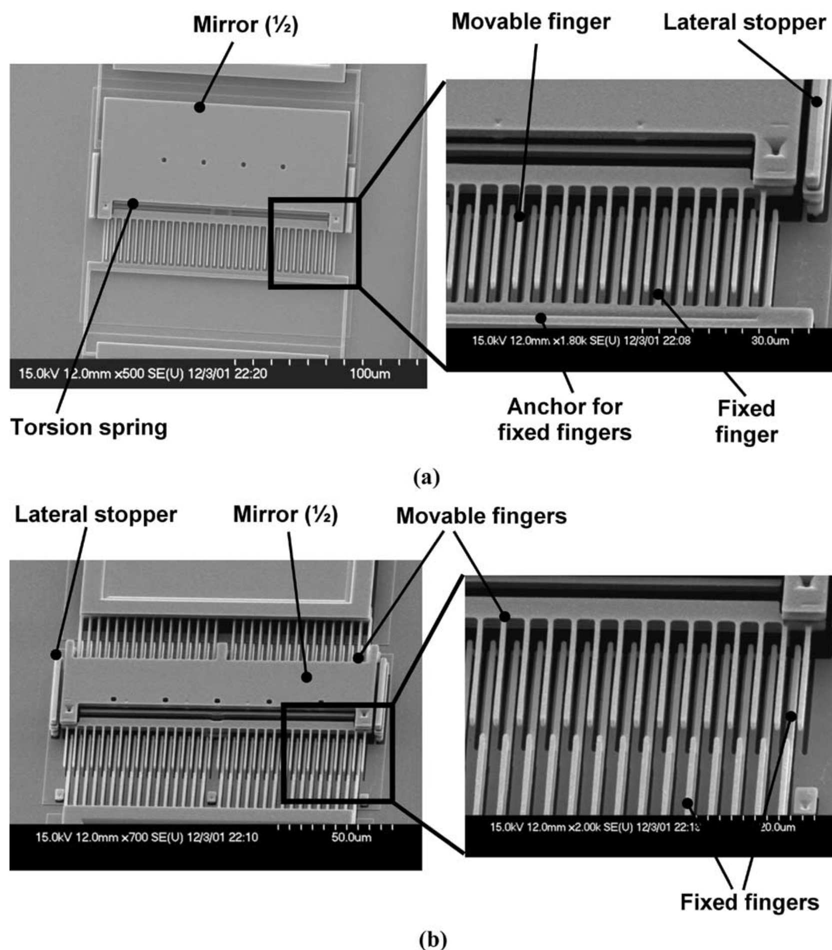

Fig. 6. The SEM micrographs of the fabricated (a) Type I micromirror $(137 \times 120\ \mu\mathrm{m}^2)$ and (b) Type II micromirror $(144 \times 60\ \mu\mathrm{m}^2)$. The lower half of the micromirror was removed intentionally to reveal the underlying comb structures. The magnified views of comb-drive parts are shown as well. Both finger gap and width are $1\ \mu\mathrm{m}$.

curvature of the micromirror could result in chromatic dispersion and wavelength-dependent loss within the passband of a channel [26]. The root-mean-square (rms) surface roughness of the mirror is measured to be 29 $\pm$ 17 nm before metallization. The metal coating increases the roughness slightly to 47 $\pm$ 29 nm, which is still less than $\lambda/20$ for $\lambda = 1550$ nm. Fig. 6 shows the scanning electron microscopy (SEM) images of the fabricated micromirrors with hidden vertical comb-drives. Half of the mirror has been removed intentionally to reveal the underlying comb structures. The movable and the fixed fingers have different contrast due to the height difference.

A. DC Scanning Characteristics

The DC scanning characteristics of the fabricated micromirrors have been measured for various finger gap spacing, finger lengths, and torsion springs by using a noncontact white light interferometric surface profiler (WYKO). The measured results (symbols) for Type I devices are shown in Fig. 7(a)–(c), together with the calculated results (lines) obtained using our hybrid FEM and pull-in model [22]. The measured results agree very well with theory. For the device with 1-μm-wide springs (single-width) and 0.5 μm finger spacing, a scan angle of 5.9° is obtained at 6 V bias [see Fig. 7(a)]. The total optical scan range is four times this angle, i.e., 23.6° (two from plus and minus angles and two from mechanical-to-optical conversion). The maximum angle is limited by vertical pull-in due to the residual parallel-plate capacitance between the mirror and the fixed fingers. As finger gap spacing increases [see Fig. 7(a)] or finger length increases [see Fig. 7(b)], the maximum continuous angle decreases because of earlier occurrence of pull-in. In all cases, measured maximum analog scan angles (or pull-in angles) are slightly lower than the calculated values. This is attributed to the narrow gaps (1 μm) between the finger tips and the bases. The largest scan angle (6.9° at 18.1 V) is realized by short comb fingers (15 μm). For comparison, the DC scanning characteristic of the parallel-plate-actuated micromirror fabricated on the same wafer with same mirror size, mirror height, and spring dimensions is also shown in Fig. 7(a). It shows a maximum analog scan angle of 3.8° with 22 V bias. In Fig. 7(c), the meander spring is three times longer than our baseline design (single-width). The required voltage bias is even lower because the meander spring is more compliant. It should be noted that all of the curves in Fig. 7(c) have similar shape. In fact, the voltage required for a given rotation angle is proportional to the square root of the spring constant

$$V = \sqrt{\frac{2k_s\theta}{\frac{\partial C_t}{\partial \theta}}}. \tag{5}$$

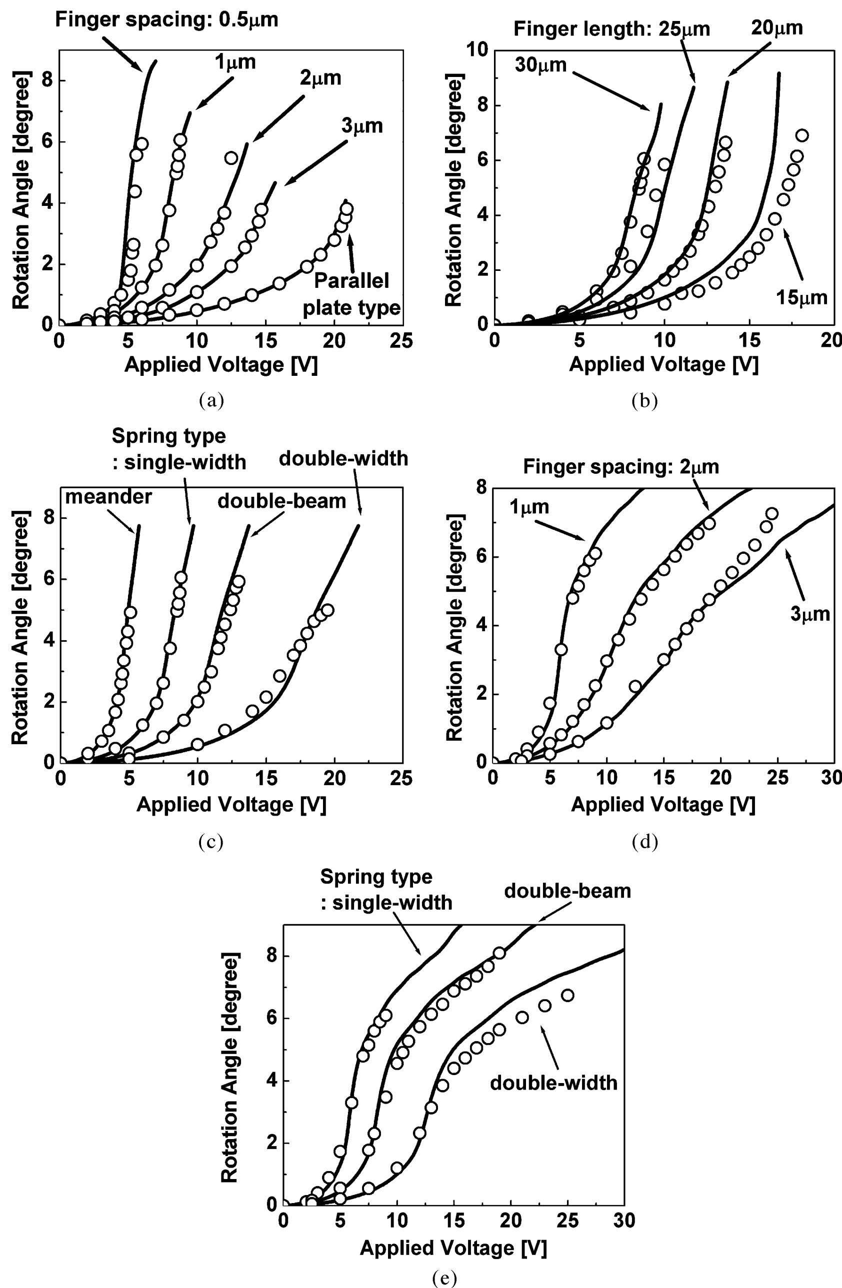

Fig. 7. The measured (circles) and calculated (lines) DC scanning characteristics of Type I devices for various (a) finger spacing, (b) finger lengths, and (c) spring types, and Type II devices for various (d) finger spacing and (e) spring types. Those of the parallel-plate-type actuator with same dimension are plotted for comparison in (a) as well. The end of each curve corresponds to the pull-in condition for all cases.

By comparing the curves in Fig. 7(c), we can obtain the ratios of measured spring constants for springs with different dimensions. Combining these with the dimensional dependence of the spring constants in (3), we can extract the amount of lateral over-etch that shrinks spring width slightly from their designed values. For example, the voltage ratio for the single-width spring and the double-width spring is 2.24. The ratio of their spring constants is $2.24^2 = 5$. Assume the amount of over-etch is uniform across the wafer, the amount of over-etching is estimated to be 0.13 μm. In other words, the width of 1-μm spring becomes 0.74 μm, and that of 2-μm spring shrinks to 1.74 μm. Finally, the shear modulus of polysilicon was extracted to be 35 GPa by curve-fitting with the measured DC scanning characteristics. This is lower than the shear modulus of single crystal silicon but is within the range of measured values reported in the literature [27]. The measured Young's modulus (E) ranges from 95 to 175 GPa. The corresponding shear modulus, $G = E/2(1+\nu)$, is between 39 GPa and 72 GPa for a Poisson's ratio (ν) of 0.22 [28]. The large spread of the measured values results from the difficulty in measuring strain or extracting the modulus from force-displacement data [27]. The shear modulus also depends on the deposition conditions of polysilicon.

The DC $\theta - V$ transfer curves of Type II devices for various finger spacing and spring designs are shown in Fig. 7(d) and (e), respectively. Again, the measured results agree very well with our calculations. The largest scan angle achieved for Type

TABLE II
DC SCANNING CHARACTERISTICS OF THE FABRICATED ANALOG MICROMIRRORS

Type	Mirror size [μm × μm]	Finger spacing [μm]	Finger length [μm]	Spring type	No. fingers	Maximum rotation angle [°]	Maximum operation voltage [V]
I	137 × 120	0.5	30	[1]*sw*	44	5.9	6.0
		1	30	*sw*	32	6.1	8.8
		2	30	*sw*	22	5.5	12.5
		3	30	*sw*	17	3.8	14.7
		1	30	[2]*db*	32	5.9	13.0
		2	30	*db*	22	4.6	18.0
		3	30	*db*	17	3.7	20.4
		1	30	[3]*dw*	32	5.0	19.5
		2	30	*dw*	22	3.6	26.0
		3	30	*dw*	17	3.1	33.0
		1	30	[4]*m*	32	4.9	5.1
		1	15	*sw*	32	6.9	18.1
		1	20	*sw*	32	6.7	13.6
		1	25	*sw*	32	5.9	10.0
II	144 × 60	1	40/29	*sw*	32	6.1	9.0
		2		*sw*	22	7.0	19.0
		3		*sw*	17	7.3	24.5
		1		*db*	32	8.1	19.0
		2		*db*	22	7.7	30.0
		3		*db*	17	6.4	34.0
		1		*dw*	32	6.7	25.0
		2		*dw*	22	6.7	42.5
		3		*dw*	17	6.3	52.5

[1]*sw*: single-width, [2]*db*: double-beam, [3]*dw*: double-width, [4]*m*: meander

II devices is 8.1° at 19 V ($\text{finger spacing} = 1\ \mu\text{m}$, double-beam springs).

Type II devices have an S-shaped characteristics while Type I devices show faster slope at large tilt angle. Hence, Type II devices are easier to control at large scan angle (near pull-in angle). However, the optical systems employing Type I devices will have smaller clipping loss because of the larger mirror areas. Usually, the mirror size needs to be twice larger than the optical beam diameter $(1/e^2)$, otherwise a significant amount of optical power will fall outside the mirror area, resulting in clipping loss. The maximum scan angle of Type II devices is limited by lateral instability (rotational pull-in about z-axis). These different pull-in mechanisms are confirmed by the 3-D profiler images taken after pull-in occurs (see Fig. 8). Table II summarizes the DC scanning characteristics of both types of devices for various design parameters.

The device with 0.5 μm finger spacing is more sensitive to misalignment between the movable and the fixed fingers. A small misalignment could lower the threshold of lateral instability. We did observe more die-to-die variation in the DC scanning characteristics for the 0.5 μm-finger-spacing devices. On the other hand, mirrors with 1 μm or larger finger spacing exhibit good uniformities.

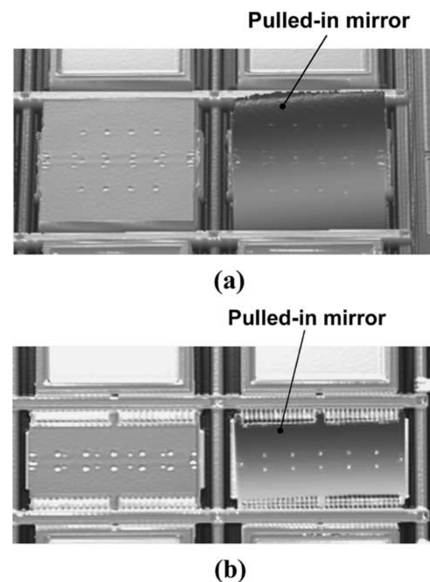

Fig. 8. The optical interferometric images of the micromirrors before (left) and after (right) pull-in. (a) Pull-in occurred to out-of-plane direction in the Type I device and (b) to in-plane direction in the Type II device.

B. Dynamic Characteristics

The resonant frequencies of the micromirrors were characterized using a Polytech laser Doppler vibrometer (LDV). The frequency response of the mirror was collected in an area-scan mode as a periodically chirped control voltage was applied to the comb-drive actuator. The measured frequency responses averaged over the scan area for various torsion springs are shown in Fig. 9. The resonant frequency is obtained from the peak of the frequency response curve. The corresponding vibration modes are also extracted from the relative responses at different parts

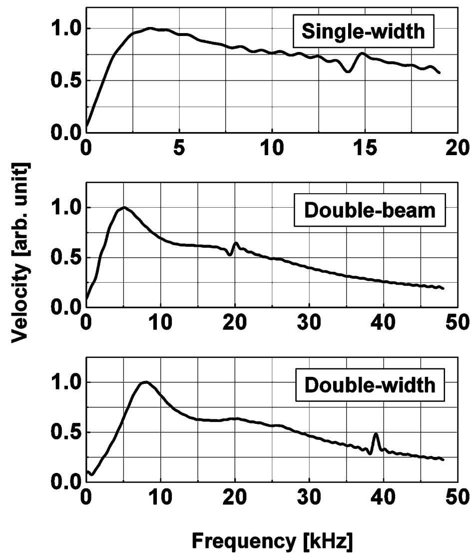

Fig. 9. Frequency responses of Type I micromirrors for various torsion springs.

TABLE III
MEASURED AND CALCULATED RESONANT FREQUENCIES OF THE ANALOG MICROMIRRORS

Spring type	Type I mirror		Type II mirror	
	Measured [kHz]	Calculated [kHz]	Measured [kHz]	Calculated [kHz]
single-width	3.4	3.5	7.7	8.0
double-beam	5.1	5.0	10.7	11.3
double-width	8.1	8.0	17.1	17.9

of the mirror. The measured resonant frequencies (f_R) for both types of devices are summarized in Table III, together with the calculated values. The ratios of the measured resonant frequencies for Type I devices are

$$f_{R,sw} : f_{R,db} : f_{R,dw} = \sqrt{k_{sw}} : \sqrt{k_{db}} : \sqrt{k_{dw}} = 1 : 1.5 : 2.4. \quad (6)$$

The resonant frequency of the rectangular mirror in rotation mode is calculated by

$$f_R = \frac{1}{2\pi}\sqrt{\frac{k_s}{I}} = \frac{1}{2\pi}\sqrt{\frac{k_s}{\frac{2}{3}\sum_i \rho_i T_i W_i L_i^3}} \quad (7)$$

where I is the total mass moment of inertia when each part has a density of ρ_i and dimensions of $T_i(\mathrm{thickness}) \times W_i(\mathrm{width}) \times L_i(\mathrm{length})$, and k_s is the torsional spring constant defined in (3). Without considering the metal coating, the calculated resonant frequencies are about 30% higher than the measured ones. Though the gold coating (0.2 μm) is much thinner than the polysilicon mirror (2.25 μm), it contributes to the mass of the mirror significantly since it is about 8 times heavier than silicon (ρ_{Au} : 19.3 $\mathrm{g/cm^3}$ and ρ_{Si} : 2.33 $\mathrm{g/cm^3}$). The measured resonant frequencies agree very well with the theoretical values taking into account the metal coating. Fig. 10(a)

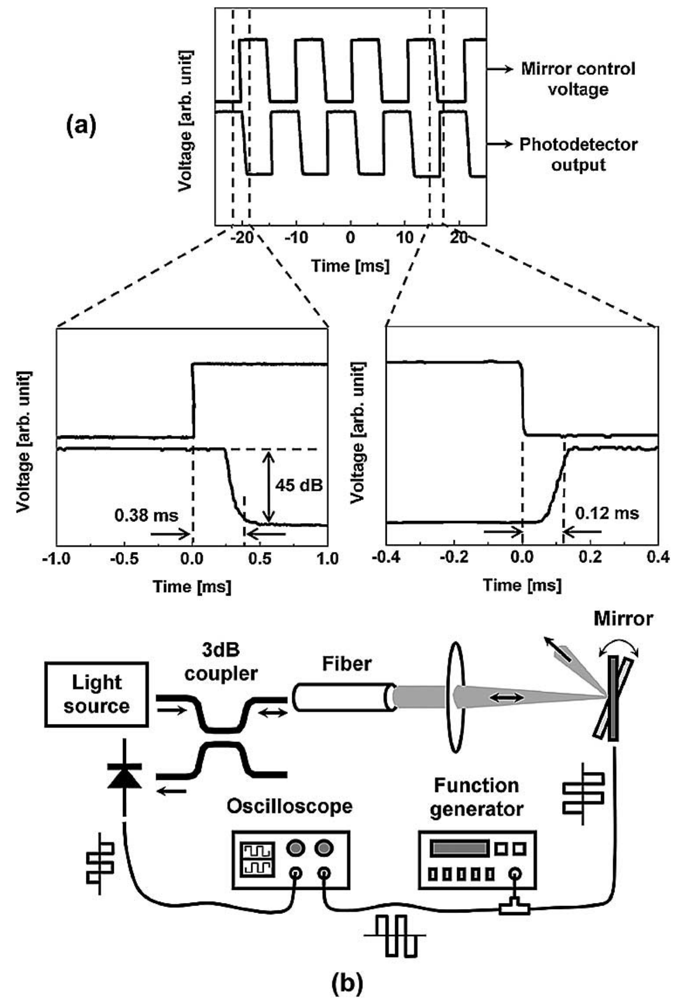

Fig. 10. (a) Temporal response of the Type I micromirror (finger spacing: $1\mu\mathrm{m}$, finger length: $30\mu\mathrm{m}$, spring type: single-width) measured by using the setup depicted in (b). The output from photodetector was measured while the control voltage was applied to the mirror. A 3-dB coupler was used to measure the reflected beam from the mirror.

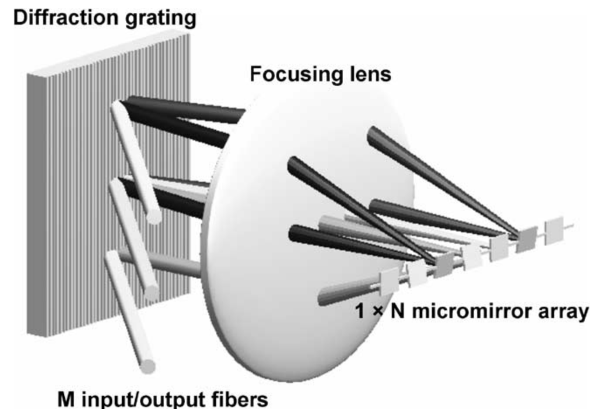

Fig. 11. Schematic diagram of the $1 \times \mathrm{M}$ wavelength selective switch using 1-D analog micromirror array. Each of N micromirror switches each wavelength, which is multiplexed/demultiplexed by a diffraction grating, among M input/output fibers.

shows the measured transient characteristics of the Type I micromirror (finger spacing: $1\mu\mathrm{m}$, finger length: $30\mu\mathrm{m}$, spring type: single-width) using the measurement setup depicted in

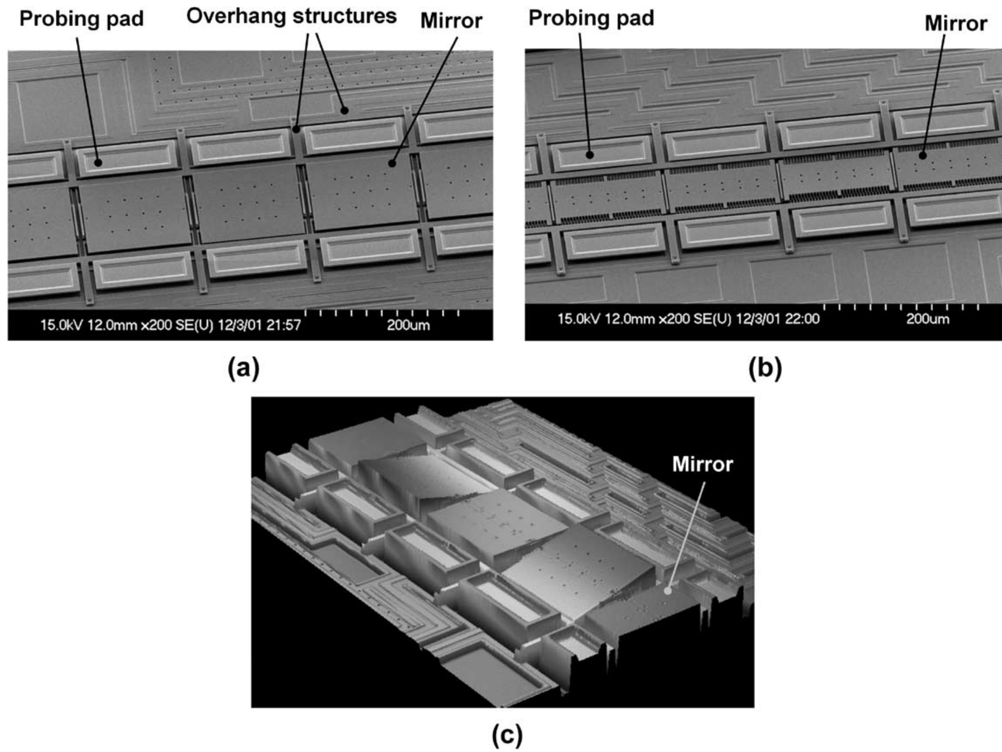

Fig. 12. SEM photographs of the 1-D analog micromirror arrays with (a) Type I (fill-factor: 91%) and (b) Type II devices (fill-factor: 96%). The mirror pitches are 150 μm for both cases. The WYKO image of the fabricated micromirror array (Type I) is shown as well (c). Two of the mirrors are tilted by biasing the actuators.

Fig. 10(b). The power of reflected light from the micromirror was measured as a square-wave voltage bias (100 Hz) was applied to the actuator. The rise and fall times are measured to be 120 and 380μs, respectively. It should be noted that these response times are for the entire optical system, which are longer than those of the mirrors alone.

IV. Micromirror Array for WDM Application

The application of analog micromirror arrays in a WDM network will be discussed in this section. Fig. 11 shows the schematic of a $1 \times \mathrm{N}$ wavelength-selective switch. Collimated input and output optical signals are demultiplexed and multiplexed by a grating spectrometer. Each wavelength is focused onto its corresponding mirror by a focusing lens. Depending on the mirror tilting angle, each wavelength can be independently sent to a different output port. This function is usually called $1 \times \mathrm{N}$ wavelength-selective switching. The SEM images of 1-D mirror arrays with Type I and Type II devices are shown in Fig. 12(a) and (b), respectively. Fig. 12(c) shows an optical interferometric image of the Type-I micromirror array. Two of the mirrors have been tilted by actuators. The angular uniformity of the array is quantified by measuring the $\theta - \mathrm{V}$ characteristics of the array, as shown in Fig. 13. The uniformity is better than ±3.2% and ±5.8% for the Type I (finger spacing: 1 μm, finger length: 30 μm, spring type: single-width) and the Type II (finger spacing: 1 μm, spring type: single-width) mirror arrays, respectively. The mechanical crosstalk between adjacent mirrors was investigated by measuring the mirror tilting angle while applying bias to the adjacent mirror. The measured crosstalk (defined as the ratio of velocities between the adjacent and the actuated mirrors) versus the bias frequency for the Type I (finger spacing: 1 μm, finger length: 30 μm, spring type: single-width) mirror array is shown in Fig. 14. It was lower than −48 dB at DC and increased slightly to −37 dB at resonance. The mechanical response from actuated mirror is plotted in Fig. 14 as a reference. There are two potential sources of crosstalk: electrical crosstalk due to inductive coupling, or electromechanical crosstalk due to fringe field of bias fingers from the adjacent actuator. Mechanical coupling through air or substrate is insignificant. The electrical crosstalk was measured to be as low as −83 dB when a sinusoidal input voltage was applied. So the main source of crosstalk is from the fringe field. This can be greatly reduced by removing the last couple of fingers at the edge of the mirror, and adding some ground shield structures between actuators. The system performance of a 1×4 wavelength selective switch using the Type I micromirror array has been reported in [24].

V. Conclusion

We have successfully designed and tested 1-D analog scanning micromirror arrays with hidden vertical comb-drive actuators. Low-operating voltage (6 V), wide scan range (23.6° optical), high fill-factor (91%), reasonably high resonant frequency (3.4 kHz), and good uniformity $(< \pm 3.2\%)$ have been demonstrated. The experimental results agree very well with our model. The application of the 1-D micromirror array to WDM wavelength-selective switches was discussed.

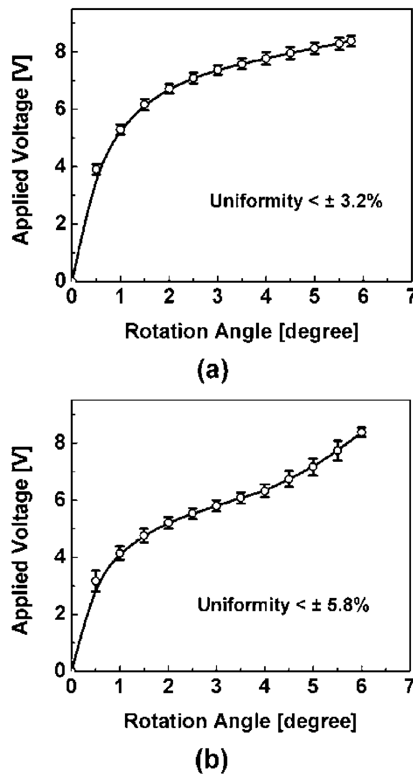

Fig. 13. Uniformities of DC scanning characteristics of the 1 × 10 analog micromirror arrays with (a) Type I (finger spacing: 1 μm, finger length: 30 μm, spring type: single-width) and (b) Type II (finger spacing: 1 μm, spring type: single-width) devices.

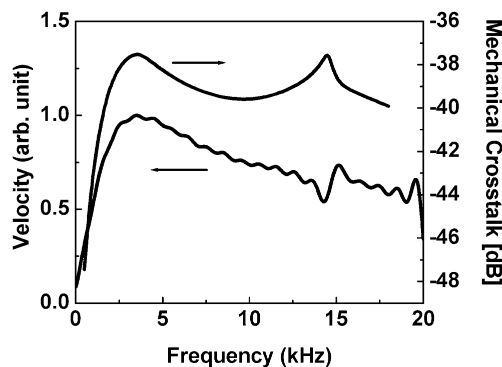

Fig. 14. Mechanical crosstalk of the micromirror array (Type I, finger spacing: 1μm, finger length: 30μm, spring type: single-width). The mechanical response from actuated mirror is plotted as well (left y-axis).

Acknowledgment

The authors would like to thank P. R. Patterson, H. Nguyen, W. Piyawattanametha, and E. K. Lau of the University of California at Los Angeles (UCLA) for their technical assistance.

References

[1] J. E. Ford, V. A. Aksyuk, D. J.David J. Bishop, and J. A. Walker, "Wavelength add-drop switching using tilting micromirrors," *J. Lightwave Technol.*, vol. 17, pp. 904–911, May 1999.
[2] L. Y. Lin, E. L. Goldstein, and R. W. Tkach, "Free-space micromachined optical switches for optical networking," *IEEE J. Select. Topics Quantum Electron.: Special Issue on Microoptoelectromechanical Systems (MOEMS)*, vol. 5, pp. 4–9, Jan.–Feb. 1999.
[3] W. Noell, L. Dellmann, C. Marxer, K. Weible, M. Hoffmann, and N. F. de Rooij, "Hybrid 4 × 4 optical cross connector based on MEMS switches and integrated optical waveguides," in *Proc. IEEE/LEOS Int. Conf. on Optical MEMS*, Okinawa, Japan, 2001, pp. 13–14.
[4] L. Fan *et al.*, "Digital MEMS switch for planar photonic crossconnects," in *Tech. Dig. Optical Fiber Conference (OFC 2002)*, Anaheim, CA, Mar. 2002, pp. 93–94.
[5] V. A. Aksyuk *et al.*, "238 × 238 micromechanical optical cross connect," *IEEE Photon. Technol. Lett.*, vol. 15, pp. 587–589, Apr. 2003.
[6] Y. Mizuno *et al.*, "A 2-axis comb-driven micromirror array for 3D MEMS switches," in *Proc. IEEE/LEOS Int. Conf. on Optical MEMS*, Lugano, Switzerland, 2002, Paper TuB4, pp. 17–18.
[7] D. M. Marom *et al.*, "Wavelength-selective 1 × 4 switch for 128 WDM channels at 50 GHz spacing," in *Tech. Dig. Optical Fiber Conference (OFC 2002)*, Anaheim, CA, Mar. 2002, Postdeadline Paper FB7.
[8] D. Hah, S. Huang, H. Nguyen, H. Chang, H. Toshiyoshi, and M. C. Wu, "A low voltage, large scan angle MEMS micromirror array with hidden vertical comb-drive actuators for WDM routers," in *Proc. Tech. Dig. Optical Fiber Conference (OFC 2002)*, Anaheim, CA, Mar. 2002, pp. 92–93.
[9] D. Hah, S. Huang, H. Nguyen, H. Chang, J.-C. Tsai, H. Toshiyoshi, and M. C. Wu, "Low voltage MEMS analog micromirror arrays with hidden vertical comb-drive actuators," in *Proc. Tech. Dig. Solid-State Sensor, Actuator, and Microsystems Workshop*, Hilton Head Island, SC, June 2002, pp. 11–14.
[10] T. Ducellier *et al.*, "The MWS 1 × 4: a high performance wavelength switching building block," in *Proc. Tech. Dig. 28th European Conference on Optical Communication (ECOC 2002)*, Copenhagen, Denmark, Sep. 8–12, 2002, Paper 2.3.1.
[11] C. Marxer, P. Griss, and N. F. de Rooij, "A multichannel variable optical attenuator for power management in fiber optic networks," in *Proc. 10th Int. Conf. Sensors and Actuators (Transducer '99)*, Sendai, Japan, June 1999, pp. 798–799.
[12] M. J. Little *et al.*, "Compliant MEMS and their use in optical components," in *Proc. Tech. Dig. Optical Fiber Conference (OFC 2002)*. CA, Mar. 2002, pp. 95–97.
[13] C. J. Chang-Hasnain, "Tunable VCSEL," *IEEE J. Select. Topics Quantum Electron.*, vol. 6, pp. 978–987, Nov. 2000.
[14] F. Sugihwo, M. C. Larson, and J. S. Harris Jr., "Micromachined widely tunable vertical cavity laser diodes," *J. Microelectromech. Syst.*, vol. 7, pp. 48–55, Mar. 1998.
[15] S. Miller, K. Turner, and N. Macdonald, "Microelectromechanical scanning probe instruments for array architectures," *Rev. Sci. Instrum.*, vol. 68, pp. 4155–4162, Nov. 1997.
[16] J.-L. A. Yeh, H. Jiang, and N. C. Tien, "Integrated polysilicon and DRIE bulk silicon micromachining for an electrostatic torsional actuator," *J. Microelectromech. Syst.*, vol. 8, pp. 456–465, Dec. 1999.
[17] R. A. Conant, J. T. Nee, K. Lau, and R. S. Muller, "A flat high-frequency scanning micromirror," in *Proc. Tech. Dig. Solid-State Sensor and Actuator Workshop*, Hilton Head, SC, 2000, pp. 6–9.
[18] J.-H. Lee, Y.-C. Ko, D.-H. Kong, J.-M. Kim, K. B. Lee, and D.-Y. Jeon, "Fabrication of silicon optical scanner for laser display," in *Proc. IEEE/LEOS Int. Conf. on Optical MEMS*, Kauai, HI, 2000, Paper MA4, pp. 13–14.
[19] U. Krishnamoorthy and O. Solgaard, "Self-aligned vertical combdrive actuators for optical scanning micromirrors," in *Proc. IEEE/LEOS Int. Conf. on Optical MEMS*, Okinawa, Japan, 2001, pp. 41–42.
[20] *http://www.mems.sandia.gov/* [Online]
[21] D. Hah, P. R. Patterson, H. Nguyen, H. Toshiyoshi, and M. C. Wu, "Theory and experiments of angular vertical comb-drive actuators for scanning micromirrors," *IEEE J. Select. Topics Quantum Electron.*, vol. 10, Mar./Apr. 2004.
[22] D. Hah, H. Toshiyoshi, and M. C. Wu, "Design of electrostatic actuators for MOEMS," in *Proc. Symp. on Design, Test, Integration and Packaging of MEMS/MOEMS (DTIP 2002)*, Cannes-Mandelieu, France, May 2002, pp. 200–207.
[23] T. Hirano, T. Furuhata, K. J. Gabriel, and H. Fujita, "Design, fabrication, and operation of submicron gap comb-drive microactuators," *J. Microelectromech. Syst.*, vol. 1, pp. 52–59, Mar. 1992.
[24] S. Huang, J.-C. Tsai, D. Hah, H. Toshiyoshi, and M. C. Wu, "Open-loop operation of MEMS WDM routers with analog micromirror array," in *Proc. IEEE/LEOS Int. Conf. on Optical MEMS*, Lugano, Switzerland, 2002, paper ThD2, pp. 179–180.
[25] R. Irwin, W. Zhang, K. Harsh, and Y. C. Lee, "Quick prototyping of flip chip assembly with MEMS," in *Proc. 1998 IEEE Radio and Wireless Conference (RAWCON 98)*, Colorado Springs, CO, Aug. 9–12, 1998, pp. 293–296.

[26] D. M. Marom, D. T. Neilson, R. Ryf, and H. R. Shea, "Effect of mirror curvature in MEMS micro-mirror based wavelength-selective switches," in *Proc. 16th Annual Meeting of the IEEE Lasers and Electro-Optics Society (LEOS 2003)*, Tucson, AZ, Oct. 26–30, 2003, pp. 305–306.
[27] W. N. Sharpe Jr, K. M. Jackson, K. J. Hemker, and Z. Xie, "Effect of specimen size on Young's modulus and fracture strength of polysilicon," *J. Microelectromech. Syst.*, vol. 10, pp. 317–326, Sep. 2001.
[28] W. N. Sharpe Jr, "Measurements of Young's modulus, Poisson's ratio, and tensile strength of polysilicon," in *Proc. MEMS 97—Tenth IEEE International Workshop on Microelectromechanical Systems*, Nagoya, Japan, 1997, pp. 424–429.

Dooyoung Hah received the M.S. and Ph.D. degrees in electrical engineering from the Korea Advanced Institute of Science and Technology (KAIST), Korea, in 1996 and 2000, respectively. His Ph.D. dissertation topic was RF MEMS switch.

From 2000 to 2001, he was a Postdoctoral Research Engineer at the University of California, Los Angeles. In 2002, he joined the Electronics and Telecommunications Research Institute (ETRI), Korea as a Senior Member of Engineering Staff. His research interests include MOEMS, RF MEMS, and micro actuators.

Dr. Hah was the third place winner at the student paper competition at 2000 IEEE MTT-S.

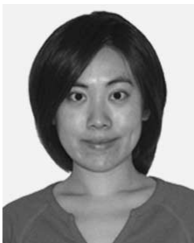

Sophia Ting-Yu Huang received the B.S. degree (*summa cum laude*) in electrical engineering from University of California, Los Angeles, in 2000 and the B.A. degree (*magna cum laude*) in management-engineering from Claremont McKenna College in 2000. She received the M.S. degree in electrical engineering with focus in photonics from University of California, Los Angeles, in 2002.

Jui-Che Tsai received the B.S. degree in electrical engineering from National Taiwan University (NTU), Taiwan, in 1997. He entered the Graduate Institute of Electro-optical Engineering at NTU after he completed his undergraduate study, and received the M.S. degree in Electro-optical Engineering in 1999. Between 1999 and 2001, he served in the military as a second lieutenant. Since 2001, he has been a Ph.D. student in Electrical Engineering at the University of California, Los Angeles.

His research interests include Optical MEMS, and optical fiber communication.

Hiroshi Toshiyoshi (M'97) received the M.Eng. and Ph.D. degrees in electrical engineering from the University of Tokyo, Tokyo, Japan, in 1993 and 1996, respectively.

In 1996, he became a Ph.D. Lecturer with Institute of Industrial Science (IIS), University of Tokyo. From April 1999 to March 2001, he stayed as a Visiting Assistant Professor at University of California, Los Angeles, for his sabbatical years. Since September 2001, he has been a Co-Director of IIS's Laboratory for Integrated MicroMechatronic Systems (LIMMS), a joint research group between IIS and Centre National de la Recherche Scientifique (CNRS), France. Since April 2002, he has been an Assistant Professor of VLSI Design and Education Center (VDEC) attached to University of Tokyo. His research interest is MEMS for free-space optics and nanomechatronics.

Ming C. Wu (S'82–M'83–SM'00–F'02) received the B.S. degree in electrical engineering from National Taiwan University in 1983 and the M.S. and Ph.D. degrees in electrical engineering and computer sciences from the University of California, Berkeley, in 1985 and 1988, respectively.

From 1988 to 1992, he was a Member of Technical Staff at AT&T Bell Laboratories, Murray Hill, NJ. In 1993, he joined the faculty of Electrical Engineering Department of the University of California, Los Angeles (UCLA), where he is currently Professor. He is also Director of UCLA's Nanoelectronics Research Facility, and Vice Chair for Industrial Relations. His current research interests include MicroElectroMechanical Systems (MEMS), Optical MEMS (MOEMS), biophotonics, microwave photonics, and high-speed optoelectronics. He has published over 340 papers, contributed to four book chapters, and holds 11 U.S. patents.

Dr. Wu was the founding Co-Chair for IEEE LEOS Summer Topical Meeting on Optical MEMS in 1996. The meeting has now evolved into IEEE LEOS International Conference on Optical MEMS that are hosted in Europe, Asia, and U.S. He has also served in program committees of many other conferences, including optical fiber communications (OFC), conference on lasers and electrooptics (CLEO), IEEE Conference on Micro Electro Mechanical Systems (MEMS), LEOS Annual Meetings (LEOS), International Electron Device Meeting (IEDM), Device Research Conference (DRC), International Solid-State Circuit Conference (ISSCC), and Microwave Photonics (MWP) Conferences. He is a David and Lucile Packard Foundation Fellow (1992–1997).